Desalination and Water Treatment
www.deswater.com

doi: 10.5004/dwt.2017.20773

78 (2017) 330–340
June

Photocatalytic enhancing for tin oxide nanoparticles by codoping with nitrogen and bismuth

R. Arunadevi[a], B. Kavitha[a], P. Pandi Sudha[a], M. Rajarajan[a,*], A. Suganthi[b,*]

[a]*P.G. and Research Department of Chemistry, C.P.A. College, Bodinayakanur 625513, India, Tel. +91-9443026532; Fax: +91-4546-280793; email: rajarajan_1962@yahoo.com (M. Rajarajan), Tel. +9789683694; email: arunarajan3@gmail.com (R. Arunadevi), Tel. +9443301264; email: kaviravee@gmail.com (B. Kavitha), Tel. +8754114071; email: pandisudharaj11@gmail.com (P. Pandi Sudha)*

[b]*P.G. and Research Department of Chemistry, Thiagarajar College, Madurai 625009, India, Tel. +91-9442035594; email: suganthicarts@gmail.com (A. Suganthi)*

Received 25 September 2016; Accepted 30 March 2017

ABSTRACT

The photocatalytic oxidation of organic dye molecules is an active area of present day's research. In this context, a new visible-light-driven photocatalyst of Bi–N codoped SnO_2 nanoparticles was prepared by hydrothermal method. The structural, morphological and optical properties were characterized by using UV–visible-diffuse reflectance spectroscopy, Fourier transform infrared spectroscopy, X-ray diffraction, scanning electron microscopy, energy dispersive X-ray spectroscopy, transmission electron microscopy, Brunauer–Emmett–Teller and X-ray photoelectron spectroscopy analysis. Bi–N codoped SnO_2 showed an enhanced photocatalytic activity for the degradation of crystal violet by facilitating electron–hole pair separation. The highest crystal violet degradation was found in 97% (with 72.8% chemical oxygen demand removal) achieved with Bi, N–SnO_2 concentration of 0.2 g/L, initial dye concentration 5 μM, pH 7 and irradiation time 180 min. Bi, N codoping in tin oxide had synergetic effect in enhancing its photocatalytic activity. The effects of doping on the SnO_2 nanoparticles included reduced energy band gap, high crystalline and small crystallite size as well as increased photocatalytic activity.

Keywords: Tin oxide; Crystal violet; Hydrothermal method; Photocatalyst

1. Introduction

Photocatalysis using metal oxide as catalysts has been widely studied for promoting degradation of organic pollutants. Over the past decade to up to date, semiconductor photocatalyst has become more and more attractive and important, since they have great potential to contribute to environmental remediation with the development of industry and economy of human society [1–3]. Among various oxide semiconductors, tin oxide (SnO_2) is one of the most promising materials to be investigated today. This is because tin oxide is a well-known n-type wide band gap (3.6 eV) semiconductor [4] and for its potential application in transparent conducting electrodes, photochemical and photoconductive devices in liquid crystal display, gas discharge display and lithium-ion batteries [5]. The valence band (VB) of SnO_2 lies at about 3.6 eV and situates at the deepest level in comparison with TiO_2, ZnO, WO_3, Fe_2O_3 and Bi_2O_3, indicating the fact that the photoholes in the VB of SnO_2 have super strong oxidative power to decompose most organic compounds. The present process, photons and energies corresponding to or exceeding the energy band gap of the semiconductor catalyst can excite electrons from the VB to the conduction band (CB), producing high-energy electron–hole pairs. SnO_2 react with water and dissolving oxygen to produce $OH^{\bullet}$ free radicals with high chemical activity

* Corresponding author.

and with the pollutant molecules adsorbed on the surface of SnO_2 photocatalyst. Recently, massive efforts have been taken to modify the photocatalytic activity of SnO_2 and make it suitable for receiving source light such as doping with nonmetals, metals and coupling with other metal oxides [6–11].

One of the most significant routes to modify the features of the SnO_2 is the introduction of dopant material in the parent system. It has been revealed that several dopants (Cr, Co, Mn, Al, Mg, Cu, Fe, Ce and La) can escort to enhance the surface area of SnO_2 nanostructure [12,13]. Anionic species such as nitrogen, carbon and sulfur were identified to potentially form new impurity levels close to the VB or CB of SnO_2, thereby lowering the band gap and shifting the absorption edge to the visible region. Codoping approaches have shown that a second element confers a synergistic sensitizing effect to nonmetal-doped SnO_2, thereby enhancing visible-light-induced photocatalytic activity. Recently, Asahi and Ohwaki [14] reported that doping TiO_2 with N could cause a narrowing in the TiO_2 band gap due to the mixing of p states of n with O 2p states of TiO_2, and hence induce visible light activity. This has been illustrated in several system such as Ag–SnO_2 [15], N–SnO_2/TiO_2 [16], Ce–Sb–SnO_2 [17], N-doped SnO_2 [18], S- or N-doped TiO_2 [19], N, La–TiO_2 [20].

However, up to now the detailed study of the structural, morphological and optical properties of hydrothermal synthesized bismuth and nitrogen codoped SnO_2 nanoparticles is still scantly. The aim of the work was to investigate and to map out the possibilities of utilizing the photocatalytic activity of Bi, N codoped SnO_2 nanoparticles for the removal of crystal violet (CV) and all of the prepared nanoparticles are found to have high photodegradation efficiency. The as-synthesized nanoparticles were characterized using UV–visible-diffuse reflectance spectroscopy (UV–Vis-DRS), Fourier transform infrared spectroscopy (FTIR), X-ray diffraction (XRD), scanning electron microscopy (SEM), energy dispersive X-ray spectroscopy (EDX), transmission electron microscopy (TEM), Brunauer–Emmett–Teller (BET) method and the average pore size determined using the Barrett–Joyner–Halenda (BJH) model and X-ray photoelectron spectroscopy (XPS) techniques. Furthermore, the photodegradation was also assessed in terms of chemical oxygen demand (COD). The effects of doping on these nanoparticles included reduced energy band gap, high crystalline of anatase phase, and small crystallite size as well as increased photocatalytic activity. The new photocatalysts have potential applications in environmental remediation. A possible mechanism for the photodegradation of CV over Bi, N–SnO_2 was also discussed in this contribution.

2. Experimental setup

2.1. Reagents

Fig. 1 shows the structure of CV. Stock solution of CV was prepared by dissolving the CV in water. All chemicals used were of reagent grade and used without further purification. Deionized, doubly distilled water was used throughout this study.

2.2. Synthesis of Bi–N–SnO_2 nanoparticles

All samples were prepared using uniform procedures. Bismuth and nitrogen doped and codoped tin oxide

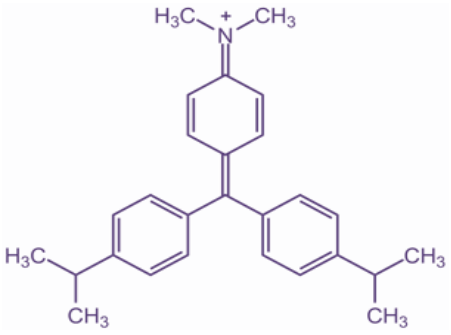

Fig. 1. Structure of crystal violet (CV).

nanoparticles have been synthesized by a hydrothermal route. 0.01 M solution of $SnCl_2.5H_2O$, $BiNO_3.5H_2O$ and urea were prepared with a molar ratio X = Bi/(Bi + Sn) and N/(N + Sn) by proper dissolving into deionized water. 15% ammonium hydroxide solution is added to the aqueous solution containing the tin chloride. Under vigorous stirring and adding concentrated HCl to adjust pH. The precipitate is refluxed for 1 h at 60°C. The resulting mixtures are allowed to stand at room temperature. Subsequently, the precipitates were washed several times with distilled water to remove residual and unwanted impurities. The final product is dried in an air hot oven at 100°C for 2 h and calcined for 2 h. Finally, the nanoparticles were calcined at 200°C for 2 h, and the samples denoted as SnO_2, Bi–SnO_2 and N–SnO_2 and Bi–N–SnO_2, respectively.

2.3. Characterization techniques

The optical properties were investigated using a UV–Vis-DRS were recorded in air at room temperature in the wavelength range of 200–800 nm using Shimadzu UV-2450 spectrophotometer. $BaSO_4$ was used as a reference with spectral reflectance standard in the wavelength range of 200–800 nm. The FTIR transmittance spectra of the samples were also analyzed using FTIR spectrometer JASCO-460 plus. The XRD measurements were carried out on a XPERT PRO X-ray diffractometer, using a Cu Kα (λ = 0.15406 nm) irradiation at 45 kV and 40 mA. SEM studies were carried out with a JSM 6701F-6701 scanning electron microscope operated to observe the surface morphology of the nanoparticles. Surface elemental composition was analyzed using an EDX attached to the SEM. TEM analysis was performed under TEM-TECNAI G2 model to observe the surface morphology, structure and grain size of the nanoparticles. The surface area was measured on approximately 250 mg of the samples using Kr at the liquid nitrogen temperature using a Micromeritics ASAP 2020 apparatus. Before the measurements, the samples were degaussed at 350°C for 18 h. The values of the surface areas were determined by the BET analysis of the physisorption isotherms. XPS measurements were taken in AXIS-NOVA system, equipped with a nonmonochromatic Al Kα (1,486.6 eV) X-ray source.

2.4. Evaluation of photocatalytic activity

CV was chosen as model pollutant. 300 mL of CV with an initial concentration of 5 μM aqueous solution and 0.2 g of

Bi–N–SnO_2 photocatalyst were fed into immersion type photoreactor; isothermal water flowing in and out through the space between the walls controlled the reaction temperature at 25°C. A xenon arc lamp operated at 300 W was used as the light source. Prior to illumination, the suspension was stirred in the dark for 30 min to achieve an adsorption–desorption equilibrium state [21–23]. Then, the suspensions containing CV and photocatalyst were irradiated using the xenon light with continuous stirring. Analytical samples were drawn from the reaction suspensions after every 10 min reaction and then centrifuged at 10,000 rpm for 10 min. The CV concentrations of the filtrates were analyzed by UV–Vis spectroscopy (400–800 nm) at its maximum absorption wavelength of 590 nm. The photodegradations of CV were calculated by the following formula:

$$\text{Photodegradation (\%)} = \frac{C_o - C}{C_o} \times 100 \quad (1)$$

where C_o is the concentration of CV before irradiation time and C is the concentration of CV after a certain irradiation time.

3. Results and discussion

3.1. XRD

The crystal structure of Bi–N–SnO_2 greatly affects its photocatalytic activity. Fig. 2 shows the XRD pattern of as-synthesized SnO_2, Bi–SnO_2, N–SnO_2 and Bi–N–SnO_2 nanoparticles calcined at 200°C for 2 h. However, the XRD patterns of the single element-doped SnO_2 (Bi–SnO_2 and N–SnO_2) and codoped SnO_2 (Bi–N–SnO_2) consists of the metal ion peaks. For SnO_2 doped with Bi and N, the diffractograms show no additional peaks that can correspond to secondary phases of the doping of nitrogen, this is because of the low concentration of nitrogen; but it is evident that the doping does not lead to drastic changes in the SnO_2 structure. For the SnO_2 all the diffraction peaks can be indexed as the typical tetragonal primitive with lattice constants in agreement with the values in the standard card (JCPDS No. 88-0287). No other diffraction peaks are detected in the SnO_2. Crystallite sizes belonging to different directions are calculated from XRD data using Scherrer's theorem. Crystallite sizes of pure SnO_2, Bi–SnO_2, N–SnO_2 and Bi–N–SnO_2 were found to be 30.86, 24.26, 17.67 and 10.42 nm, respectively. The average particle size of all the nanoparticles was tabulated in Table 1. The crystallite size was decreased on codoped SnO_2 comparing with SnO_2 and doped SnO_2 nanoparticles. The crystalline sizes were estimated from XRD peaks using the Scherrer equation [24]:

$$D = \frac{K\lambda}{\beta Cos\theta} \quad (2)$$

where D is crystalline size, K is the shape factor equals to 0.89, λ is the wavelength of X-ray radiation (Cu Kα = 0.15406 nm), β is the angle with at half maximum height and θ is the half diffraction angle.

3.2. UV–Vis-DRS

The spectra were taken in the wavelength range of 200–800 nm for studying the optical properties of the SnO_2, Bi–SnO_2, N–SnO_2 and Bi–N–SnO_2 as-synthesized nanoparticles were shown in Fig. 3(a). The band gap energy values of different samples were calculated using the Tauc's relation [25,26]:

$$\alpha h\nu = A\left(h\nu - E_g\right)^n \quad (3)$$

where n is a constant which depends on the probability of transition; it takes the values n = 1/2 for indirect allowed transitions, respectively. Fig. 3(b) shows variation of $(\alpha h\nu)^2$ vs. $h\nu$, the straight line in the higher energy domain,

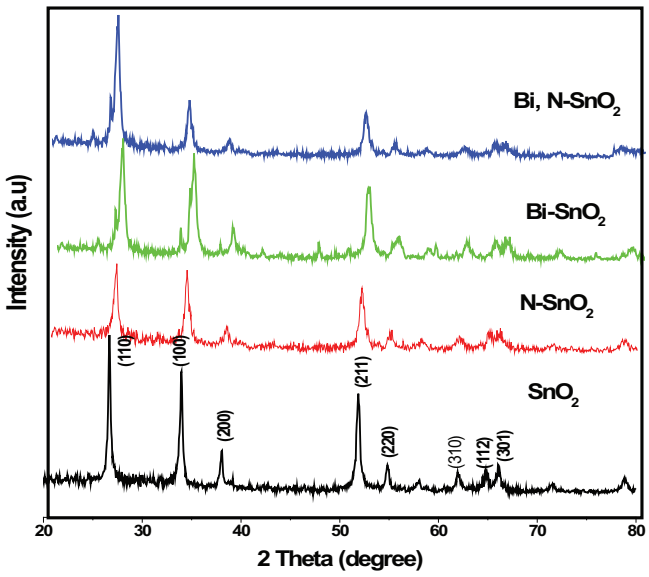

Fig. 2. XRD patterns of SnO_2, Bi–SnO_2, N–SnO_2 and Bi–N–SnO_2.

Table 1
XRD particle size (nm), TEM particle size, band gap (E_g, eV), surface area (m^2/g) and morphology of SnO_2, Bi–SnO_2, N–SnO_2 and Bi–N–SnO_2

Samples	XRD particle size (nm)	TEM particle size (nm)	Band gap, E_g (eV)	Surface area (m^2/g)	Morphology
SnO_2	30.86	–	3.32	16.02	Uniform, global and slightly agglomerated with nanoaggregates
Bi–SnO_2	24.26	–	3.15	35.73	
N–SnO_2	17.67	–	2.79	35.06	
Bi–N–SnO_2	10.42	11.0	2.59	140.43	

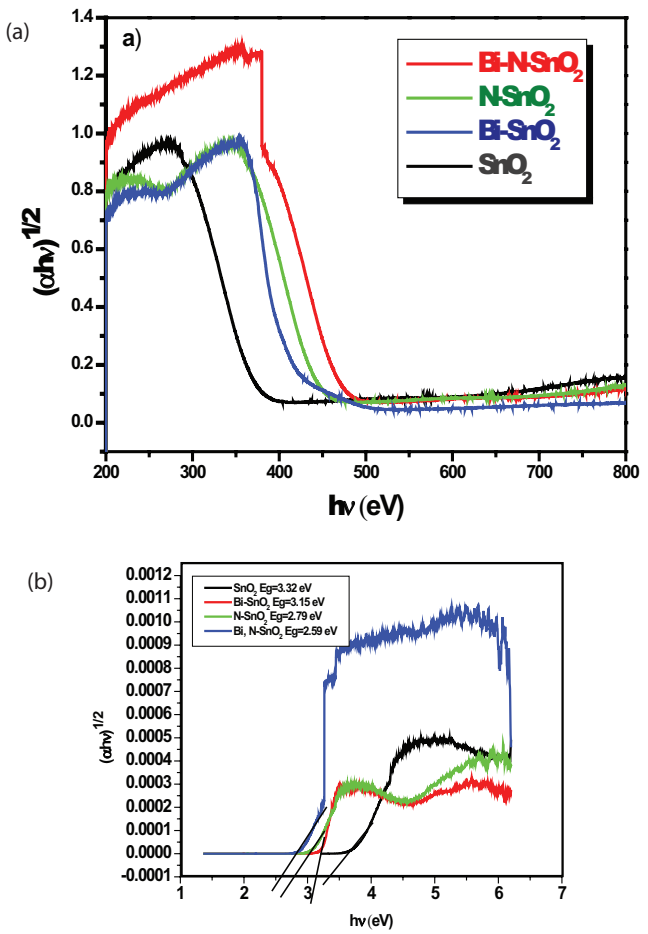

Fig. 3. (a) UV–Vis-DRS spectrum of SnO_2, Bi–SnO_2, N–SnO_2 and Bi–N–SnO_2. (b) Tauc plot of SnO_2, Bi–SnO_2, N–SnO_2 and Bi–N–SnO_2 nanoparticles.

indicating a direct optical transition. The band gap energy E_g was obtained by extrapolating the linear portion of the graph to energy axis at $\alpha = 0$. The dopants affected the UV–Vis-DRS spectra by inhibiting recombination of electron–hole pairs, especially in the case of N doping. The major effect of N doping on the absorption spectra enhanced absorption at long wavelength regions (>500 nm) in the N-doped SnO_2, which might be useful in enhancing the photocatalytic visible light activities of these materials. An increasing amount of Bi led to higher absorbencies in the visible region, emphasizing the synergistic effect of codoping in enhancing visible light activity. The optical band gaps were 3.32, 3.15, 2.79 and 2.59 eV for the pure SnO_2, Bi–SnO_2, N–SnO_2 and Bi–N–SnO_2 nanoparticles, respectively. The narrow band gap, caused by localized N 2p states in the band structure in the form of substitutional and interstitial N states, allowed the enhancement of visible light photocatalytic activity. After Bi and N codoping to the SnO_2, the photoabsorptions of photocatalyst enhanced specifically in the range of 400–800 nm. It could be seen that the red shift in UV–Vis spectra divulge the visible range absorption with Bi and N codoped SnO_2.

3.3. SEM–EDX and TEM

Figs. 4(a)–(d) show the overall surface morphology of SnO_2, doped and codoped SnO_2 nanoparticles. The figures reveal that the SnO_2 compound consists of large aggregates these are transformed to finer aggregates on doping bismuth and nitrogen. The images show the agglomeration of homogeneous particles with a size distribution of around 1 μm in diameter. The SEM investigations of all samples reveal the crystallites nature of nanoparticles.

Figs. 5(a)–(d) show the EDX spectra of the prepared products, the elemental composition of the samples such as Sn, Bi, N and O are examined using EDX analysis, which confirm the availability of dopants Bi and N on the SnO_2

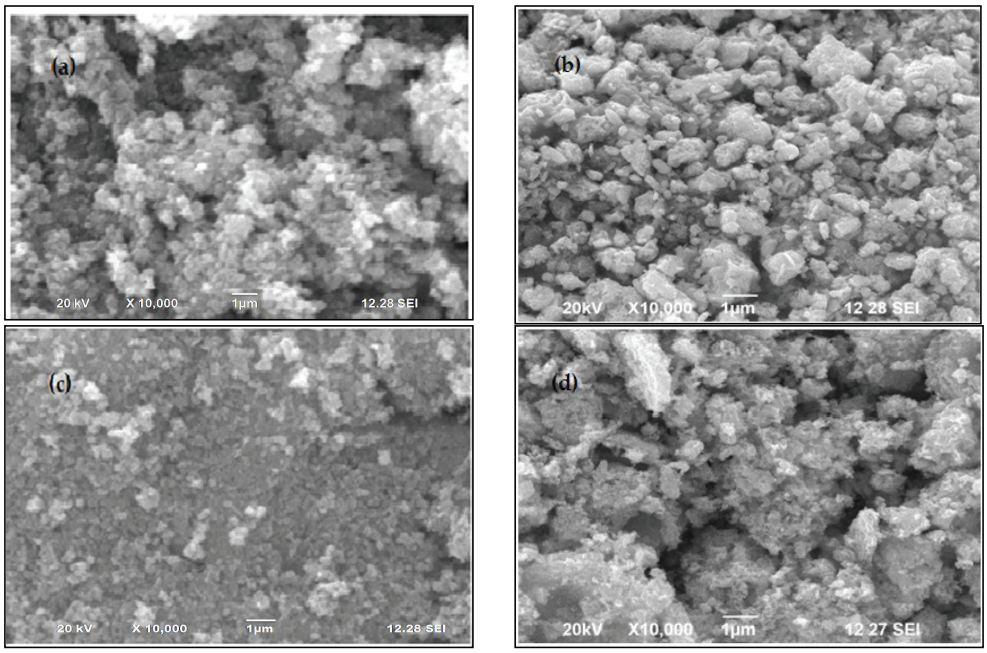

Fig. 4. SEM image of (a) SnO_2, (b) Bi–SnO_2, (c) N–SnO_2 and (d) Bi–N–SnO_2.

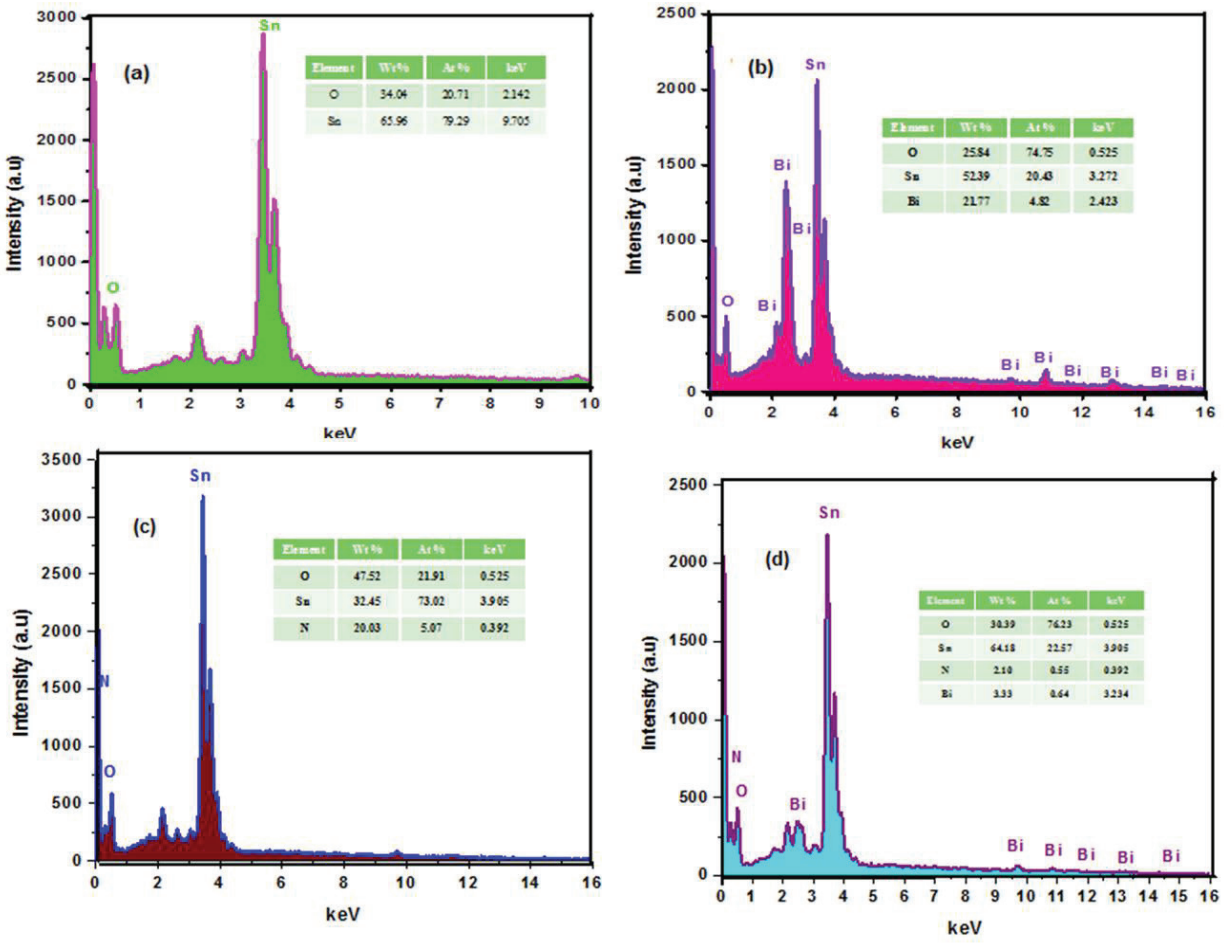

Fig. 5. EDX data of (a) SnO_2, (b) Bi–SnO_2, (c) N–SnO_2 and (d) Bi–N–SnO_2.

matrix. It could be observed that Bi and N had been successfully doped in the SnO_2 crystal lattice. The atomic percentage of Bi and N are almost equal to their nominal stoichiometry within the experimental error.

Fig. 6 shows typical TEM images of Bi–N–SnO_2 nanoparticles. It was obvious from TEM micrographs that the morphology of the particles are found to be nearly spherical in shape and form the images it is also evident that in the present synthesized samples agglomeration was decreased with uniform distribution of particles by the doping of Bi and N to the host matrix. The average size of nanoparticles obtained from TEM analysis is in the range of 11.0 nm, which is slightly higher than the crystallite size calculated from XRD spectra.

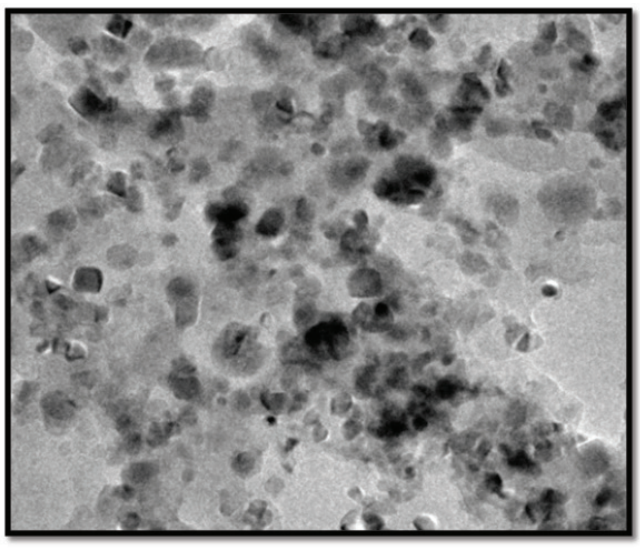

Fig. 6. TEM image of Bi–N–SnO_2.

3.4. BET analysis

Figs. 7(a)–(d) show the BET specific surface areas of the SnO_2, Bi–SnO_2, N–SnO_2 and Bi–N–SnO_2 nanoparticles and the values are reported in Table 1. The surface area of SnO_2, Bi–SnO_2, N–SnO_2 and Bi–N–SnO_2 for 16.02, 35.73, 35.06 and 140.43 m^2/g, respectively. Undoubtedly codoping led to the enhancement of the BET surface area. Moreover the codoping had an influence on the surface area of SnO_2 photocatalysts. As in the literature, the reaction of photocatalytic activity that occurs on the surface area of photocatalyst affects the reaction rate. The codoped SnO_2 nanoparticles follow the type-IV isotherms indicating that the samples have mesoporous structure [27]. High specific surface area of Bi,

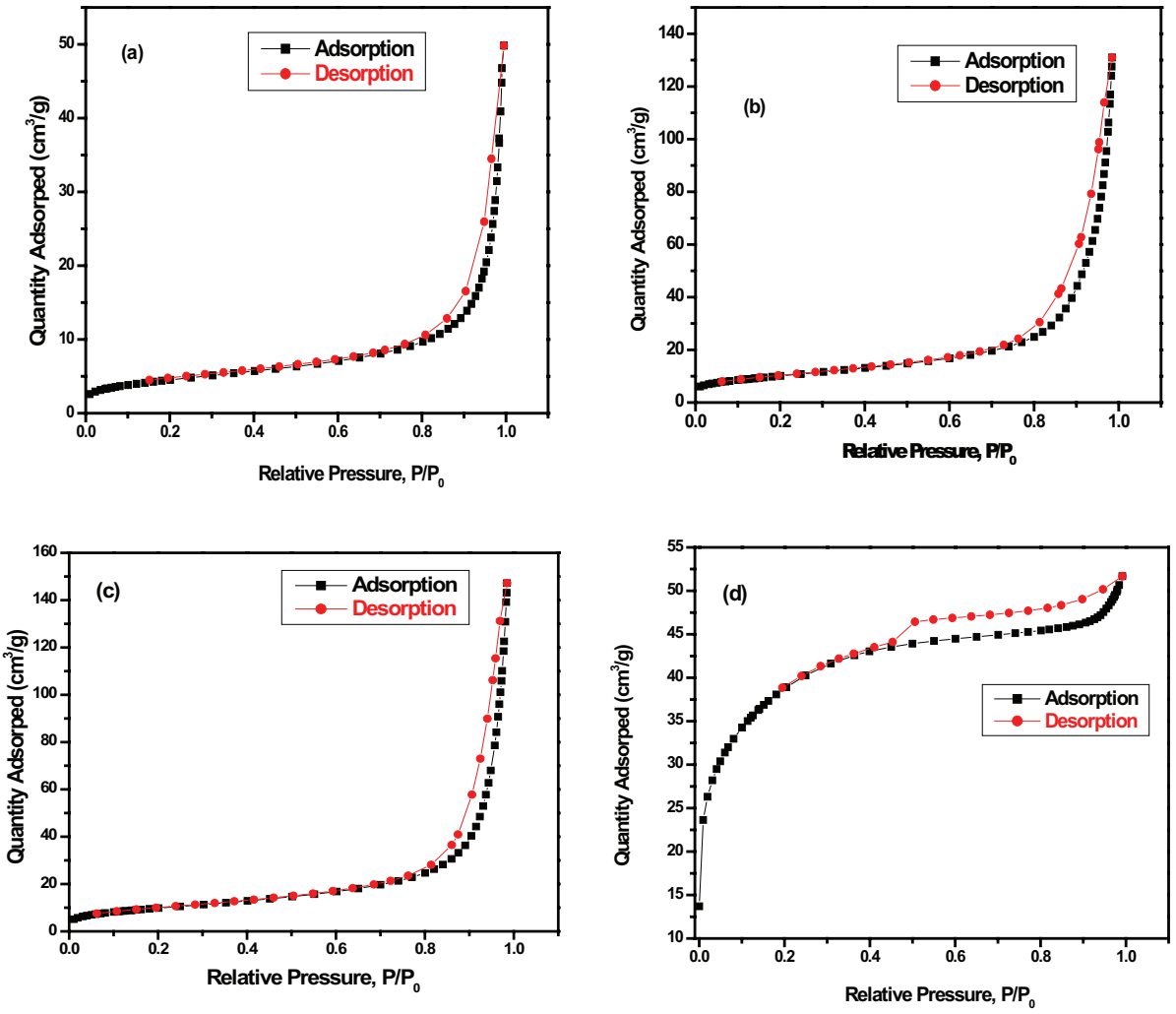

Fig. 7. The BET specific surface areas of the SnO_2, Bi–SnO_2, N–SnO_2 and Bi–N–SnO_2 nanoparticles.

N–SnO_2 will provide more active site for the photocatalytic reaction with dye molecules and enhance the interfacial reaction process. This phenomenon favors the enhancement in photocatalytic activity [28,29].

3.5. XPS

Figs. 8(a)–(d) represent the XPS spectrum of Sn 3d, O 1s, Bi 4f and N 1s in synthesized Bi–N–SnO_2. It is used to investigate the elemental composition and chemical states of bismuth, nitrogen, oxygen and tin. The peaks at 485.34 and 491.06 eV in Fig. 8(a) can be attributed to Sn $3d_{5/2}$ and $3d_{3/2}$ of SnO_2 while the peak at 530.81 eV (Fig. 8(b)) belongs to O 1s of SnO_2. The peaks at 165.19 and 159.9 eV (Fig. 8(c)) can be assigned to Bi $4f_{7/2}$ and $4f_{5/2}$ whereas the peaks at 403.13 eV (Fig. 8(d)) is attributed to N 1s in Bi–N–SnO_2.

3.6. Measurement of photocatalytic activity

The photodegradation of CV is used to evaluate the photocatalytic activity of SnO_2, Bi–SnO_2, N–SnO_2 and Bi–N–SnO_2 nanoparticles. The photocatalytic activities of all the samples under visible light irradiation are shown in Fig. 9. The photodegradation was also measured in dark and in the absence of catalyst, the degradation is negligible. Vignesh et al. [30] demonstrated the increment in surface area of nanoparticles could make the more photoactive site then smaller one, the time required for adsorption–desorption equilibrium between the pollutant and photocatalyst was 30 min. We observed that the changes of photocatalytic activity of Bi–N codoped SnO_2 are attributed to the Bi–N structure and oxygen vacancy. First, because the oxygen vacancies give rise to the local states below the conduction edge and the interstitial N atoms induce the local states near the VB edge, both the doped atoms and the O_2 vacancies in the lattice of SnO_2 can extend its light absorption from UV to visible range. CV with an initial concentration of 5 μM under visible light for various irradiation times. The results revealed that the metal and nonmetal codoped SnO_2 showed higher photocatalytic activity than that of Bi–N–SnO_2. In addition, photocatalytic activity of the prepared nanoparticles can be ranged in the following order: Bi–N–SnO_2 > Bi–SnO_2 > N–SnO_2 > SnO_2 that is Bi–N–SnO_2 nanoparticles displayed highest photocatalytic of 97% for CV can be degraded in 180 min. The ultimate

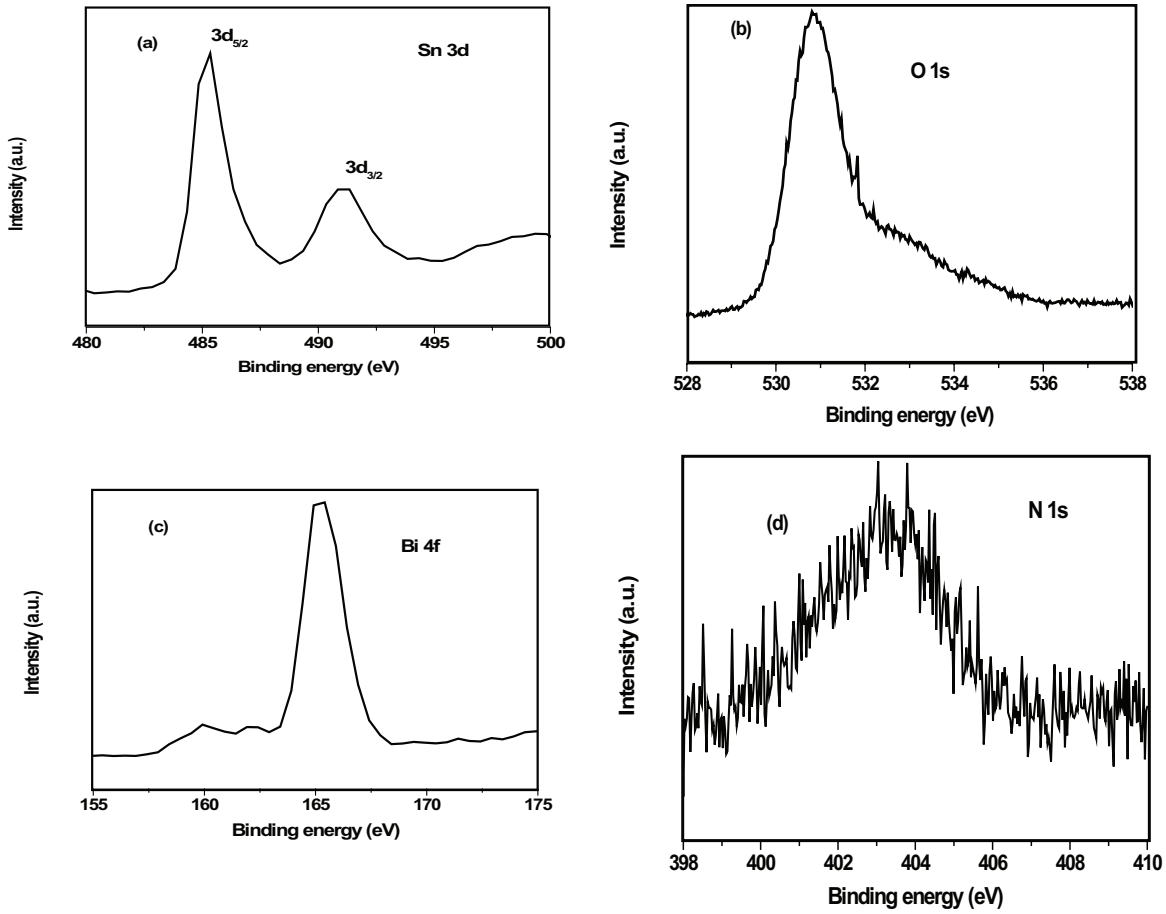

Fig. 8. XPS spectra of Bi–N–SnO_2 nanoparticles (a) Sn 3d, (b) O 1s, (c) Bi 4f and (d) N 1s.

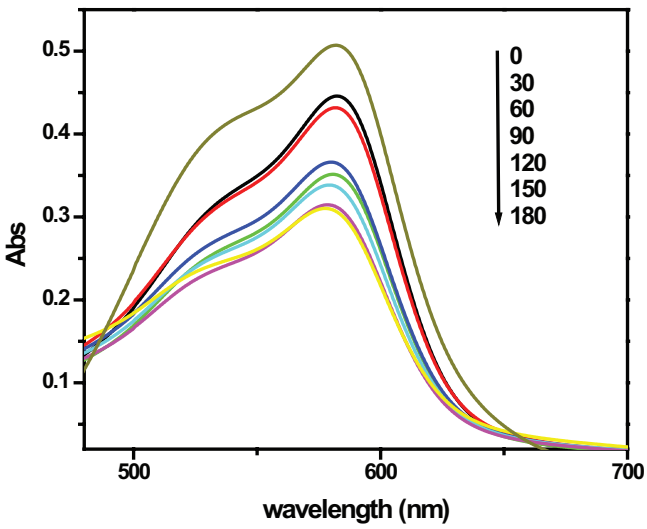

Fig. 9. Time dependent UV–Vis spectral changes of CV in the presence of Bi–N–SnO_2 under visible light irradiation.

photocatalytic activity is obtained in the codoped SnO_2 nanoparticles, which can be explained due to the synergistic effects of Bi and N doping. The amount of CV was plotted as a function of irradiation time. It is clear, that the photodegradation of CV in the presence of the Bi–N–SnO_2 led to the degradation of the compound in Fig. 10. The degradation of the 590 nm absorption band suggests the chromophore responsible for the characteristic color of the dye was being broken down. The photodegradation of CV in the presence of the prepared catalyst follows pseudo-first-order kinetic equation and it can be expressed as follows [31]:

$$-\ln(C/C_0) = kt \quad (4)$$

where C_0 is the initial concentration of CV at $t = 0$ min, C is the concentration of CV at irradiation time t and k is the rate constant. The plot of $-\ln(C/C_0)$ vs. irradiation time t is depicted in Fig. 11. And a linear relationship is observed. The rate constant (k) was calculated from the slopes and it was found to be 1.0×10^{-3} s^{-1}, 3.0×10^{-3} s^{-1}, 6.0×10^{-3} s^{-1} and 2.3×10^{-2} s^{-1} for SnO_2, Bi–SnO_2, N–SnO_2 and Bi–N–SnO_2, respectively.

3.7. Mechanism of degradation

As mechanistic scheme of the photocatalytic degradation by Bi–N–SnO_2 photocatalysts is shown in Fig. 12. When semiconductor is illuminated by UV irradiation, a VB electron goes to CB leaving a hole in VB. Generally, these

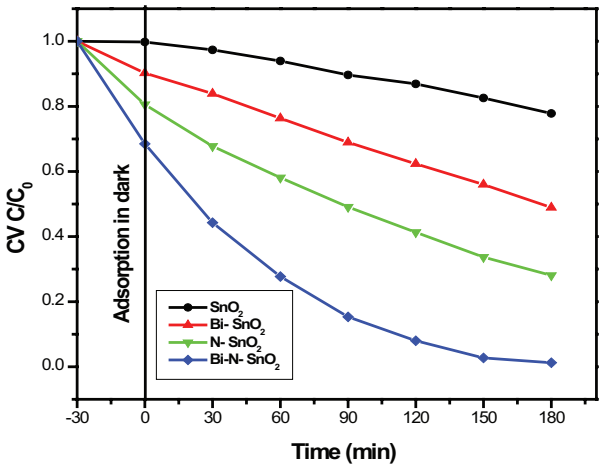

Fig. 10. Effect of SnO_2, Bi–SnO_2, N–SnO_2 and Bi–N–SnO_2 on the photodegradation of CV.

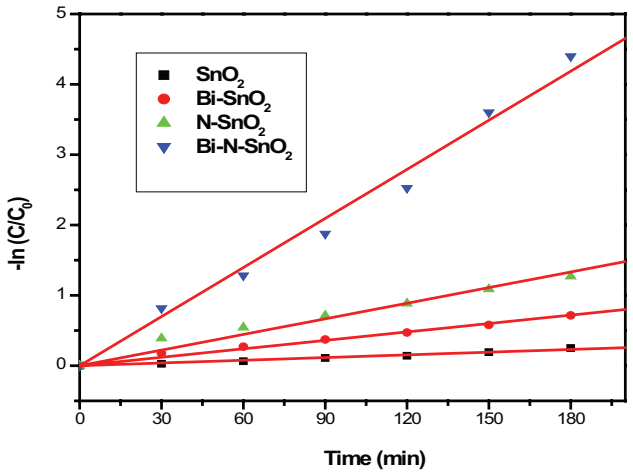

Fig. 11. Kinetic plot of $-\ln(C/C_0)$ vs. irradiation time for the photodegradation of CV.

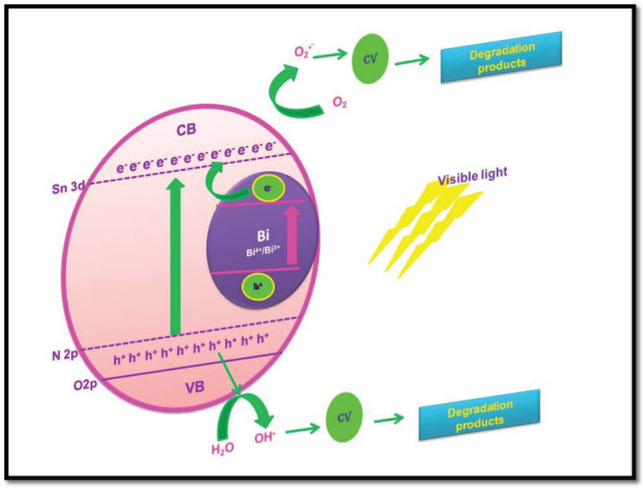

Fig. 12. Proposed visible-light-induced photocatalytic mechanism of Bi–N–SnO_2.

electron–holes are recombined to reduce the photocatalytic activity of semiconductors. But the presence of Bi and N trap the electron from CB of SnO_2. Simultaneously, it suppresses the electron–hole recombination. It is well established that Bi traps the electrons from CB of SnO_2. The 'N' doping also expresses the electron–hole recombination by electron trapping. In N-doped SnO_2 interband-gap states are formed above the VB. The holes generated migrate to the surface where they scavenge water molecules or OH ions to form OH radicals mineralize any adsorbed organic molecules. The trapped electrons by Bi and N product more number of superoxide radical anion and at the same time VB holes of SnO_2 react with water is produce highly reactive hydroxyl (OH) radical. The superoxide radical anion and hydroxyl radical are used for the degradation of dye. The doping Bi as Bi^{4+}/Bi^{3+} presented on the surface of N–SnO_2 photocatalysts can act as electron traps and enhance the charge separation and further improve the photocatalytic activity of Bi–N–SnO_2 predominantly. The synergistic effects of Bi and N doping, in which the N doping cause the visible light response and improves the quantum yield and photocatalytic activity of SnO_2, and Bi doping cause the enhancement of the separation of photogenerated charge carriers [32].

3.8. Effect of Bi–N–SnO_2 dosage

In order to optimize the dosage of catalyst, experiments were carried out with from 0.125 to 0.25 g/L, at constant CV concentration of 5 μM and the results were shown in Fig. 13. The photodegradation efficiency of CV is negligible (5.15%) without addition of photocatalyst during 180 min irradiation. The photodegradation of CV increases with increase of catalyst from 0.125 to 0.20 g/L. This is due to the increase of total active surface area and the availability of more active sites on the catalyst surface for photoreaction. However, the high catalyst dosage (0.25 g/L) increases the turbidity of the suspension, leading to a shielding effect on the penetration of light. Therefore, the absorption of light by the catalyst is limited and the surface area also reduced due to agglomeration of the catalyst at high catalyst dosage [33,34].

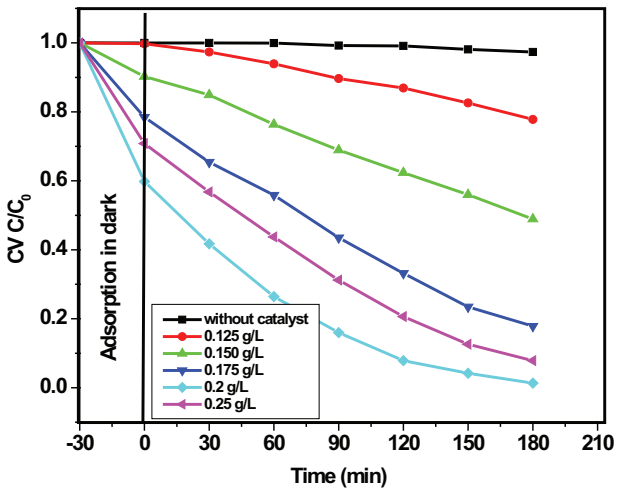

Fig. 13. Effect of dosage on the photodegradation of CV.

3.9. Effect of pH in photodegradation

pH is an important factor that influences the photodegradation process. The effect of pH on the photodegradation of CV was studied in the range of 5–9 with an initial CV concentration of 5 μM and Bi–N–SnO_2 dosage of 0.2 g/L and the results were displayed in Fig. 14. The photodegradation of CV increases when the pH is increased from 5 to 7 and then decreases at the pH 9. This is due to the change in electrostatic attraction or repulsion between dye molecules and catalyst. CV is a cationic dye and therefore the electrostatic attraction between the dye molecules and catalyst is greatly improved at pH 7 [35]. The adsorption of H_2O molecules at the semiconductor surface followed by the dissociation –OH groups, leading to coverage with chemically equivalent metal hydroxyl group (M–OH) [36].

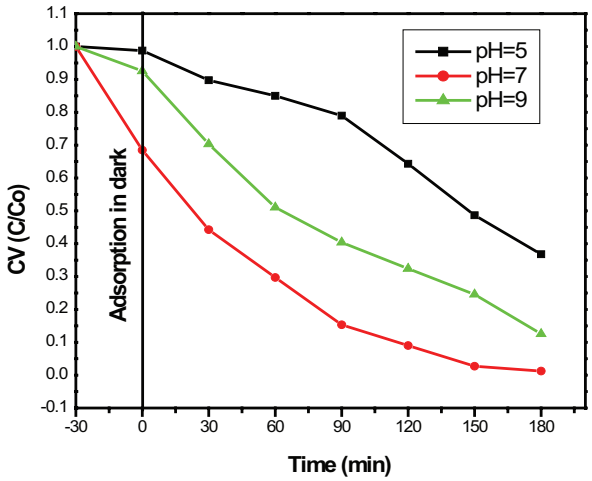

Fig. 14. Effect of pH on the photodegradation of CV.

3.10. Effect of initial dye concentration

The effect of initial CV concentration was investigated in the presence of 0.2 g/L of Bi–N–SnO_2 at a pH 7 by varying concentration from 5 to 15 μM is displayed in Fig. 15. As the initial CV concentration increases, the degradation percentage decreases. This is due to the following reasons: at high dye concentration, the generation of active species on the photocatalyst surface is reduced because the active sites are completely covered by the dye molecules. According to Beer–Lamberts law the path length of photons entering into the dye solution decreases. The generation of reactive species also remains constant at fixed catalyst concentration.

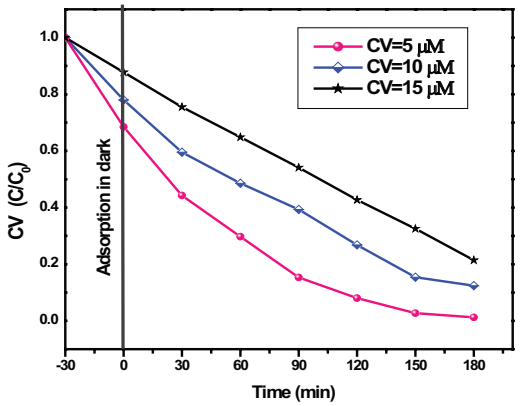

Fig. 15. Effect of initial CV concentration and its photodegradation.

3.11. COD analysis

The COD is commonly used as an effective technique to assess the degree of mineralization reached during the photocatalytic treatment [37]. The COD was determined by standard dichromate method [38] and the results are shown in Fig. 16. Also, COD removal efficiency of the CV under optimized conditions (CV concentration 5 μM, catalyst dosage 0.2 g/L, pH 7) was studied at the reaction time of 180 min and 72.8% COD removal efficiency was obtained. The experimental result might be interpreted by assuming that most of the solute was completely mineralized in the photocatalytic process. Moreover, the removal of the COD does not also embody completely the mineralization of CV. The results indicated that, during the photodecolorization process, most of organic matter degrades to smaller species (especially inorganic compounds) and hence the required COD decreases [39]. The percentage removal efficiency was calculated by the following formula

$$\%\ \text{of COD removal} = \frac{[\text{COD}_{\text{blank}} - \text{COD}_{\text{CV}}]}{\text{COD}_{\text{blank}}} \times 100 \quad (5)$$

The BET surface area of codoped photocatalysts was higher compared with single element dopant, thus giving higher available sites for adsorption and degradation reaction to take place. It was observed that Bi–N–SnO_2 photocatalyst displayed the highest COD removal. During the photocatalytic process, the absorbed photon energy excites the electron in the VB and transferred it to the CB, leaving a hole in the VB.

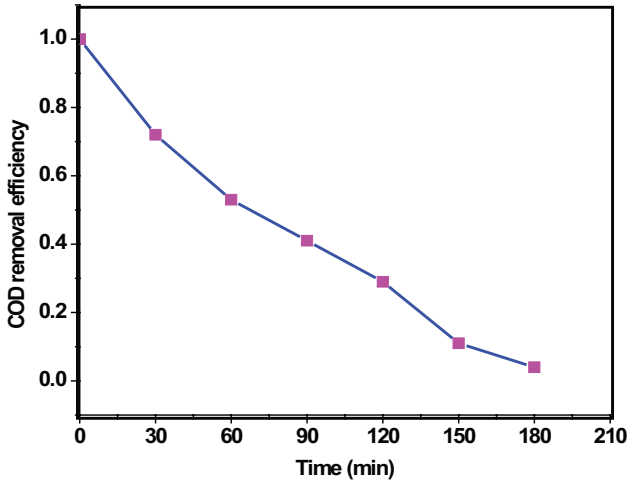

Fig. 16. COD removal.

Table 2
Comparison with other catalysts

Catalyst	Model pollutant	Light source	Contact time	% of degradation	Reference
Iodine-doped tin oxide (SnO_2:I)	Phenol	UV and sunlight	150 min	93.4	[40]
Chlorophyll sensitized C/SnO_2	Toluidine blue	Visible light	45 min	68.30	[41]
Ti-doped SnO_2	Methylene blue	UV and visible-light	135 min	92	[42]
SnO_2	Methyl violet 6B	Sun light	240 min	99.1	[43]
Bi–N–SnO_2	Crystal violet	Visible light	180 min	97	Present work

3.12. Comparison with other catalysts

Various SnO_2 modified catalysts for removal of pollutant in water were reported in literature [40–43] and the present investigation are summarized in Table 2.

4. Conclusion

In order to enhance the visible light photocatalytic activity of Bi–N–SnO_2 nanoparticles for practical environmental remediation, a facile hydrothermal method for the degradation of CV in water. The Bi and N can act as electron mediator to effectively inhibit the recombination of photogenerated electron/hole pairs. The UV–Vis-DRS analysis shows that the codoping of Bi and N into SnO_2 shifts the absorption band of SnO_2 from UV to visible region and the band gap energy is reduced for codoped catalysts (from 3.32 to 2.59 eV), the largest reduction gap was observed for codoped catalysts. SEM and EDX studies were done to fully analyze the surface morphology and elemental composition of the Bi–N–SnO_2 nanoparticles having uniform agglomeration. Also, EDX and XPS results confirm the existence and atomic percentage of all elements present in the as-synthesized catalyst. Bi–N–SnO_2 nanoparticles in the size range of 11.0 nm were observed in TEM image. The structure of the obtained tetragonal SnO_2 nanoparticles was also characterized by XRD and FTIR analysis. The average particle size of tetragonal nanoparticles obtained by the XRD analysis is 10.42 nm. This is good agreement with TEM observation. The UV–Vis absorption spectra demonstrated the quantum confinement effect. The photocatalytic activity measurement demonstrates that the Bi–N–SnO_2 photocatalysts show superior photoactivity in degradation of CV under visible light irradiation.

Acknowledgments

The author (RA) gratefully acknowledged the financial support obtained from the Tamil Nadu government, Department of collegiate education (RC. No. 8760/K2/2014). Furthermore, the authors want to thank the management of Cardamom Planters' Association College for providing necessary facilities to carry out this work.

Symbols

C_0	—	Concentration of dye before irradiation time
C	—	Concentration of dye after irradiation time
D	—	Crystalline size
K	—	Shape factor
λ	—	wavelength of X-ray
β	—	Angle with at half maximum height
θ	—	Diffraction angle
α	—	Adsorption coefficient
$h\nu$	—	Light frequency
A	—	Constant
k	—	Rate constant
t	—	Time

References

[1] E.S. Jang, J.H. Won, S.J. Hwang, J.H. Choy, Fine tuning of the face orientation of ZnO crystals to optimize their photocatalytic activity, Adv. Mater., 18 (2006) 3309–3312.
[2] T.J. Kuo, C.N. Lin, C.L. Kuo, M.H. Huang, Growth of ultralong ZnO nanowires on silicon substrates by vapor transport and their use as recyclable photocatalysts, Chem. Mater., 19 (2007) 5143–5147.
[3] B.X. Li, Y.F. Wang, Facile synthesis and enhanced photocatalytic performance of flower-like ZnO hierarchical microstructures, J. Phys. Chem. C., 114 (2010) 890–896.
[4] L.C. Nehru, V. Swaminathan, C. Sanjeeviraja, Photoluminescence studies on nanocrystalline tin oxide powder for optoelectronic devices, Am. J. Mater. Sci., 2 (2012) 6–10.
[5] A. Kay, M. Gratzel, Dye-sensitized core−shell nanocrystals: improved efficiency of mesoporous tin oxide electrodes coated with a thin layer of an insulating oxide, Chem. Mater., 14 (2002) 2930–2953.
[6] Y. Wang, **C.-m. Fan**, B. Hua, Z.-h. Liang, Y.-p. Sun, Photoelectrocatalytic activity of two antimony doped SnO_2 films for oxidation of phenol pollutant, Trans. Nonferrous Met. Soc. China, 19 (2009) 778–783.
[7] X. Hui-li, Z. Hui-sheng, Z. Tao, X. Dong-chang, Photocatalytic degradation of Acid Blue 62 over CuO-SnO_2 nanocomposite photocatalyst under simulated sun light, J. Environ. Sci., 19 (2007) 1141–1145.
[8] S. Pan, S. Wang, Y. Zhang, S. Xu, F. Kong, Y. Luo, Y. Tian, X. Teng, G. Li, Surface Fe^{3+}-decorated pristine SnO_2 nanoparticles with enhanced ·OH radical generation performance, Catal. Commun., 24 (2012) 96–99.
[9] R. Sasikala, A. Shirole, V. Sudarsan, T. Sakuntala, C. Sudakar, R. Naik, S.R. Bharadwaj, Highly dispersed phase of SnO_2 on TiO_2 nanoparticles synthesized by polyol-mediated route: photocatalytic activity for hydrogen generation, Int. J. Hydrogen Energy, 34 (2009) 3621–3630.
[10] L.P. Zhu, N.C. Bing, D.D. Yang, Y. Yang, G.H. Liao, L.J. Wang, Synthesis and photocatalytic properties of core–shell structured α-Fe_2O_3@SnO_2 shuttle-like nanocomposite, J. Cryst. Eng. Commun., 13 (2011) 4486–4490.
[11] H. Xia, H. Zhuang, T. Zhang, D. Xiao, Visible-light-activated nanocomposite photocatalyst of Fe_2O_3/SnO, Mater. Lett., 62 (2008) 1126–1128.
[12] M.M. Rahman, A. Jamal, S.B. Khan, M. Faisad, Highly sensitive ethanol chemical sensor based on Ni-doped SnO_2 nanostructure materials, Biosens. Bioelectron., 28 (2011) 127–134.
[13] Z. Jiang, Z. Guo, B. Sun, Y. Jia, M. Li, J. Liu, Highly sensitive and selective butanone sensors based on cerium-doped SnO_2 thin films, Sens. Actuators, *B*, 145 (2010) 667–673.

[14] R. Asahi, T. Ohwaki, Visible-light photocatalysis in nitrogen-doped titanium oxide, Science, 293 (2001) 269–271.
[15] K. Vignesh, R. Hariharan, M. Rajarajan, A. Suganthi, Photocatalytic performance of Ag doped SnO_2 nanoparticles modified with curcumin, Solid State Sci., 21 (2013) 91–99.
[16] P. Kongsong, L. Sikong, S. Niyomwas, V. Rachpech, Photocatalytic antibacterial performance of glass fibers thin film coated with N-doped SnO_2/TiO_2, Sci. World J., 2014 (2014) 869–706.
[17] H. Liu, K. Zhao, T. Wang, J. Deng, H. Zeng, Facile preparation of cerium (Ce) and ntimony (Sb) codoped SnO_2 for hydrogen production in lactic acid solution, Mater. Sci. Semicond. Process., 40 (2015) 670–675.
[18] X. Sun, R. Long, X. Cheng, X. Zhao, Y. Dai, B. Huang. Structural, electronic, and optical properties of N-doped SnO_2, J. Phys. Chem. C, 112 (2008) 9861–9864.
[19] T. Ohno, Z. Miyamoto, K. Nishijima, Sensitization of photocatalytic activity of S- or N-doped TiO_2 particles by adsorbing Fe^{3+} cations, Appl. Catal., A, 302 (2006) 62–68.
[20] H. Wei, Y. Wu, N. Lun, F. Zhao, Preparation and photocatalysis of TiO_2 nanoparticles co-doped with nitrogen and lanthanum, J. Mater. Sci., 39 (2004) 1305–1308.
[21] K. Vignesh, A. Suganthi, B.-K. Min, M. Rajarajan, M. Kong, Designing of YVO4 supported β-AgI nanophotocatalyst with improved stability, RSC Adv., 5 (2015) 576–585.
[22] M. Hojamberdiev, G. Zhu, P. Sujaridworakun, S. Jinawath, P. Liu, J.P. Zhou, Visible-light-driven N–F-codoped TiO_2 powders derived from different ammonium oxofluorotitanate precursors, Powder Technol., 218 (2012) 140–148.
[23] T. Sun, J. Fan, E. Liu, L. Liu, Y. Wang, H. Dai, Y. Yang, W. Hou, X. Hu, Z. Jiang, Fe and Ni co-doped TiO_2 nanoparticles prepared by alcohol-thermal method: application in hydrogen evolution by water splitting under visible light irradiation, Powder Technol., 228 (2012) 210–218.
[24] M.M.B. Mohaghehi, N. Shahtahmasebi, M.R. Alinejad, A. Youssefi, M.S. Saremi, The effect of the post-annealing temperature on the nano-structure and energy band gap of SnO_2 semiconducting oxide nano-particles synthesized by polymerizing–complexing sol–gel method, Physica B, 403 (2008) 2431–2437.
[25] W. Zeng, T. Liu, D.J. Han, Hydrogen sensing and mechanism of M-doped SnO_2 (M = Cr^{3+}, Cu^{2+} and Pd^{2+}) nanocomposite, Sens. Actuators, B, 160 (2011) 455–462.
[26] C.Y. Wang, S.Y. Ma, F.M. Li, Y. Chen, X.L. Xu, T. Wang, F.C. Yang, Q. Zhao, J. Liu, X.L. Zhang, X.B. Li, X.H. Yang, J. Zhu, The effect of Mg and Al co-doping on the structural and photoelectric properties of ZnO thin film, Mater. Sci. Semicond. Process., 17 (2014) 27–32.
[27] X.Z. Ding, X.H. Liu, Correlation between anatase-to-rutile transformation and grain growth in nanocrystalline titania powder, J. Mater. Res., 13 (1998) 2556–2559.
[28] K. Vignesh, M. Kang, Facile synthesis, characterization and recyclable photocatalytic activity of Ag_2WO_4@g-C_3N_4, Mater. Sci. Eng., B, 199 (2015) 30–36.
[29] B.S. Kwak, K. Vignesh, N.-K. Park, H.-J. Ryu, J.-I. Baek, M. Kang, Methane formation from photoreduction of CO_2 with water using TiO_2 including Ni ingredient, Fuel, 143 (2015) 570–576.
[30] K. Vignesh, S. Kang, B.S. Kwak, M. Kang, Meso-porous ZnO nanotriangles @ graphitic-C_3N_4 nano-foils: fabrication and recyclable photocatalytic activity, Sep. Purif. Technol., 147 (2015) 257–265.
[31] M. Stylidi, D.I. Kondarides, X.E. Verykios, Pathways of solar light-induced photocatalytic degradation of azo dyes in aqueous TiO_2 suspensions, Appl. Catal., B, 40 (2003) 271–286.
[32] Q.M. Kang, B.L. Yuan, J.G. Xu, M.L. Fu, Synthesis, characterization and photocatalytic performance of TiO_2 codoped with bismuth and nitrogen, Catal. Lett., 141 (2011) 1371–1377.
[33] S. Anandan, A. Vinu, N. Venkatachalam, B. Arabindoo, V. Murugesan, Photocatalytic activity of ZnO impregnated Hβ and mechanical mix of ZnO/Hβ in the degradation of monocrotophos in aqueous solution, J. Mol. Catal. A: Chem., 256 (2006) 312–320.
[34] J.Z. Kong, A.D. Li, X.Y. Li, H.F. Zhai, W.Q. Zhang, Y.P. Gong, H. Li, D. Wu, Photo-degradation of methylene blue using Ta-doped ZnO nanoparticles, J. Solid State Chem., 183 (2010) 1359–1364.
[35] L.N. Tong, X.M. He, H.B. Han, J.L. Hu, A.L. Xia, Y. Tong, Effects of H_2 annealing on ferromagnetism of Ni-doped ZnO powders, Solid State Commun., 150 (2010) 1112–1116.
[36] M.C. Neve, J.M.F. Nogneira, T. Trindade, M.H. Mendonca, M.I. Pereira, O.C. Monteiro, Photosensitization of TiO_2 by Ag_2S and its catalytic activity on phenol photodegradation, J. Photochem. Photobiol., A, 204 (2009) 168–173.
[37] D. Fabbri, A. Bianco Prevot, F. Pramauro, Effect of surfactant microstructures on photocatalytic degradation of phenol and chlorophenols, Appl. Catal., B, 62 (2006) 21–27.
[38] R.Y. Hong, J.H. Li, L.L. Chen, D.Q. Liu, H.Z. Li, Y. Zheng, J. Ding, Synthesis, surface modification and photocatalytic property of ZnO nanoparticles, Powder Technol., 189 (2009) 426–432.
[39] K. Vignesh, R. Hariharan, M. Rajarajan, A. Suganthi, Visible light assisted photocatalytic activity of TiO_2–metal vanadate (M¼Sr, Ag and Cd) nanocomposites, Mater. Sci. Semicond. Process., 16 (2013) 1521–1530.
[40] A.M. Al-Hamdi, M. Sillanpää, J. Dutta, Photocatalytic degradation of phenol by iodine doped tin oxide nanoparticles under UV and sunlight irradiation, J. Alloys Compd., 618 (2015) 366–371.
[41] M.S. Solanki, R. Ameta, S. Benjamin, Sensitization of carbon doped Tin (IV) oxide nanoparticles by chlorophyll and its application in photocatalytic degradation of Toluidine blue, Int. J. Adv. Chem. Sci. Appl., 3 (2015) 24–30.
[42] L. Ran, D. Zhao, X. Gao, L. Yin, Highly crystalline Ti-doped SnO_2 hollow structured photocatalyst with enhanced photocatalytic activity for degradation of organic dyes, Cryst. Eng. Commun., 17 (2015) 4225–4237.
[43] A. Bhattacharjee, M. Ahmaruzzaman, T. Sinha, A novel approach for the synthesis of SnO_2 nanoparticles and its application as a catalyst in the reduction and photodegradation of organic compounds, Spectrochim. Acta, Part A, 136 (2015) 751–760.